Journal of Nanobiotechnology

RESEARCH

Open Access

5-FU@HFn combined with decitabine induces pyroptosis and enhances antitumor immunotherapy for chronic myeloid leukemia

Zuowei Yuan[1,2†], Guoyun Jiang[1,3†], Ying Yuan[4†], Qian Liang[5], Yaxin Hou[6], Wenyao Zhang[1], Lujia Tang[1], Kelong Fan[5,6*] and Wenli Feng[1*]

Abstract

Background Tyrosine kinase inhibitors (TKIs) constitute the primary treatment for chronic myeloid leukemia (CML). However, resistance to TKIs often leads to treatment failure. Pyroptosis, a form of programmed cell death, has emerged as a promising strategy in cancer therapy due to its ability to eliminate tumor cells while stimulating antitumor immunity. Low-dose decitabine (DAC) has been shown to reverse methylation-induced silencing of the pyroptosis-related gene gasdermin E (GSDME) in some tumor cells, offering a potential new therapeutic option for CML. Herein, we propose a combination therapy using 5-fluorouracil (5-FU), a broad-spectrum chemotherapeutic agent, and low-dose DAC to induce pyroptosis in CML cells via the caspase-3/GSDME pathway. However, the nonspecific targeting of 5-FU diminishes its pyroptosis efficacy and causes off-target toxicity, highlighting the need for a targeted drug delivery system.

Results In this study, we developed 5-FU@HFn nanoparticles (NPs) by loading 5-FU into the recombinant human heavy chain ferritin (HFn) nanocage through a high-temperature via the drug channels on the protein cage. The loading efficiency was approximately 50.62 ± 1.17 μg of 5-FU per mg of HFn. 5-FU@HFn NPs selectively targeted CML cells through CD71-mediated uptake, significantly enhancing the therapeutic effects of 5-FU. When combined with DAC, 5-FU@HFn NPs effectively activated pyroptosis via the caspase-3/GSDME pathway in both TKI-sensitive and TKI-resistant CML cells. In a CML mouse model, this combination therapy significantly suppressed tumorigenesis and triggered a robust antitumor immune response, facilitating the clearance of leukemic cells. Furthermore, the 5-FU@HFn NPs exhibited excellent in vivo safety.

Conclusions The innovative therapeutic strategy, combining 5-FU@HFn nanoparticles with low-dose DAC, effectively induces caspase-3/GSDME-mediated pyroptosis and activates antitumor immunity for CML. This approach offers a potential alternative for patients resistant or intolerant to TKIs.

†Zuowei Yuan, Guoyun Jiang and Ying Yuan contributed equally to this work.

*Correspondence:
Kelong Fan
fankelong@ibp.ac.cn
Wenli Feng
fengwl@cqmu.edu.cn

Full list of author information is available at the end of the article

Graphical abstract

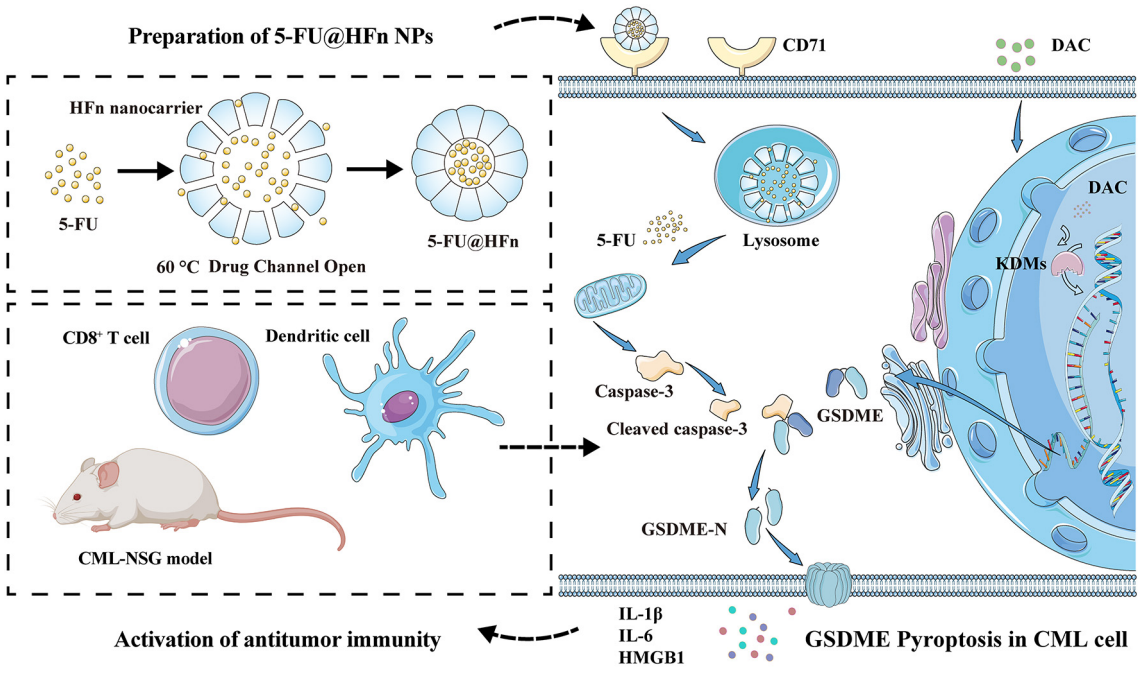

Keywords Chronic myeloid leukemia, Ferritin nanocage, 5-fluorouracil, Pyroptosis, Antitumor immunity

Background

Chronic myeloid leukemia (CML) is a myeloproliferative malignancy originating from abnormal hematopoietic stem cells (HSCs) [1]. CML is characterized by the formation of the BCR/ABL oncogene, which results from a reciprocal translocation between chromosomes 9 and 22, known as the Philadelphia chromosome [2]. The current standard treatment for CML involves tyrosine kinase inhibitors (TKIs), which specifically target the BCR/ABL fusion protein [3]. While TKIs achieve molecular remission in 40–70% of patients, 15–25% develop resistance or intolerance [4]. Additionally, TKIs are ineffective against leukemia stem cells (LSCs), leaving residual disease even in patients who achieve complete hematologic remission, thereby contributing to relapse [5, 6]. Although allogeneic hematopoietic stem cell transplantation (HSCT) remains the most effective option for TKI-resistant and relapsed cases, its application is limited by donor availability, high costs, and severe complications such as acute graft-versus-host disease (GVHD) [7]. Thus, there is an urgent need to explore alternative therapeutic strategies for CML.

Pyroptosis, an inflammatory form of programmed cell death mediated by gasdermin (GSDM) proteins, has emerged as a promising cancer therapy approach [8, 9]. It is characterized by rapid cell swelling, membrane pore formation, and the release of pro-inflammatory factors, including lactate dehydrogenase (LDH), interleukin-1β (IL-1β), interleukin-6 (IL-6), and high mobility group box 1 (HMGB1) [10]. Unlike apoptosis, pyroptosis not only eliminates tumor cells but also activates antitumor immunity, making it an attractive therapeutic strategy [11–13]. However, inducing pyroptosis requires high GSDM expression and activation, which are often silenced in cancer cells, including CML cells [14]. Decitabine (DAC), a DNA methyltransferase (DNMT) inhibitor, has been shown to upregulate gasdermin E (GSDME) at low-dose in certain cancers [15–17]. GSDME, encoded by the *DFNA5* gene [18], converts caspase-3-dependent apoptosis into pyroptosis upon cleavage [13, 19–21]. Our preliminary experiments confirmed that low-dose DAC effectively increased GSDME expression in CML cells. Upon caspase-3 activation by chemotherapeutic agents, upregulated GSDME is cleaved into its N-terminal fragment (GSDME-N), which induces pyroptosis. 5-Fluorouracil (5-FU), a widely used chemotherapeutic agent, triggers the caspase-3-dependent apoptotic pathway in various cancer cells, including CML [22]. Based on these findings, we hypothesize that combining 5-FU with low-dose DAC may effectively induce pyroptosis in CML cells. However, the nonspecific cytotoxicity of 5-FU limits its therapeutic efficacy, leading to adverse effects such as gastrointestinal toxicity, bone marrow suppression, neurotoxicity, and liver damage [23–25]. Therefore,

targeted delivery of 5-FU to tumor cells is critical to maximizing its therapeutic potential while minimizing systemic toxicity.

With the rapid advancement of nanotechnology, nanocarriers have emerged as promising platforms for targeted drug delivery. Ferritin, a natural carrier of inorganic minerals, self-assembles into a 24-mer spherical nanocage with an outer diameter of approximately 12 nm and an internal cavity of about 8 nm [26]. Its unique structural and self-assembly properties make it an ideal vehicle for small-molecule drug delivery [27–29]. Recombinant human heavy-chain ferritin (HFn) has been identified as an effective drug delivery vehicle in cancer therapy due to its specific binding to transferrin receptor 1 (CD71), which is overexpressed in various cancers, including leukemia [30, 31]. Based on this, we attempted to load 5-FU into HFn to construct a targeted nanodrug delivery system for CML cells.

In this study, we successfully developed a 5-FU@HFn nanoparticles (NPs) delivery system. When combined with low-dose DAC, 5-FU@HFn efficiently induced caspase-3/GSDME-mediated pyroptosis in CML cells in vitro and in vivo. Furthermore, this combination therapy triggered a robust antitumor immune response, providing a safe and effective therapeutic strategy for CML, particularly for patients resistant or intolerant to TKIs.

Methods

Materials and cell lines

HFn was produced through prokaryotic expression in *Escherichia coli* based on our past report [27]. The CML cell lines used were K562 and its TKI-resistant variant K562/G01, which were preserved in our laboratory. 5-fluorouracil (5-FU) and decitabine (DAC) were purchased from Sigma–Aldrich (USA) and Abmole (USA), respectively.

Preparation of 5-FU@HFn NPs

5-FU was loaded into the HFn nanocage via natural drug entry channels on the protein cage at high temperatures, as described in our previous researches [27, 32]. In detail, HFn proteins (in 50 mM Tris-HCL, pH 8.0, 2.0 mg/mL) and 5-FU (in DMSO, 0.5 mg/mL) were mixed and incubated at 60 °C for 8 h. Then, the purified 5-FU@HFn nanoparticle products were obtained by further centrifugation via a 100 kDa centrifugal filter unit (Millipore, USA) to remove free 5-FU. The optimal conditions for preparing 5-FU@HFn were determined by varying the incubation temperature (40 °C to 70 °C), incubation time (1 h to 16 h), and mass ratio of HFn/5-FU (0.5:1 to 8:1). Furthermore, the thermal stability of 5-FU was evaluated at 60 °C. The morphological properties of 5-FU@HFn were visualized and photographed by transmission electron microscopy (TEM, FEI Tecnai, USA), and the sizes were determined by dynamic light scattering (DLS) size analyzer (Brookhaven, USA).

5-FU loading efficiency

5-FU was quantified via high-performance liquid chromatography (HPLC) with an Agilent 1260 system (Agilent, Germany) and a Welch Ultimate® AQ-C18 column (Welch, China). The concentration of 5-FU in the ultrafiltrate from the centrifugal filter unit was determined via HPLC, and the amount of loaded 5-FU per mg of HFn was calculated as follows: (total mass of 5-FU) – (mass of 5-FU in ultrafiltrate)/(total mass of HFn). The HPLC detection parameters included a wavelength set at 265 nm, a temperature of 25 °C, a flow rate of 1.0 mL/min, an injection volume of 20 μL, and a detection time of 8 min. The mobile phase comprised 97% HPLC grade methanol and 3% phosphate buffer (50 mM). A standard curve for 5-FU detection was generated using 5-FU standard solutions ranging from 1 to 20 μg/mL.

Drug release of 5-FU@HFn

To assess drug release efficiency from the 5-FU@HFn NPs in the intracellular environment, we added 1 mg of 5-FU@HFn to 1 mL of PBS at pH 7.4 or 5.0. The mixture was incubated at 37 °C with shaking at 100 rpm and subsequently centrifuged at 4,000 rpm for 10 min via a 100 kDa centrifugal filter unit (Millipore, USA) at 12, 24, 48, 72, and 96 h. The ultrafiltrate was collected, and the concentration of 5-FU in the ultrafiltrate was determined via HPLC. The cumulative release rate of 5-FU was calculated according to the concentration of 5-FU released at each time point.

Blood compatibility assay

Fresh blood from human or mice was collected and centrifuged at 3,000 rpm for 5 min to isolate red blood cells (RBCs), washed with sterile saline solution until the suspension became colorless, and resuspended in sterile saline at a 2% hematocrit. A mixture containing 0.9 mL of the 2% RBC suspension and 0.1 mL of either 5-FU@HFn or HFn solution at various concentrations was prepared. A positive control was established using 0.9 mL of the 2% RBC suspension and 0.1 mL of 10× Red Blood Cell Lysate (Raisecare, China); the negative control contained 0.1 mL of saline. After the mixtures were incubated for 1 h at 37 °C, they were centrifuged at 3,000 rpm for 5 min, and the supernatant was transferred to a 96-well plate. The absorbance (A) was then measured at 540 nm via a microplate reader (Bio-Tek, USA). The hemolysis rate was calculated via the following formula:

$$hemolysis\ rate\ (\%) = (A\,5 - FU@HFn\ or\ A\,HFn\ -\ A\ negative) /(A\ positive\ -\ A\ negative)\ \times\ 100\%$$

5-FU@HFn labeled with Cy5

A total of 10 mg of 5-FU@HFn and 0.5 mg of red-fluorescent dye Cyanine5 (Cy5) (MCE, USA) were thoroughly mixed in a 100 mM $NaHCO_3$ solution at pH 8.3, and the mixture was incubated at room temperature in the dark for 12 h. The mixture was subsequently transferred to a 100 kDa centrifugal filter unit (Millipore, USA) and centrifuged at 4,000 rpm for 10 min to remove any unbound Cy5. Following this, an equal volume of PBS was added to the filter unit and washed 10 times under the same centrifugation conditions. Finally, the filter unit was inverted and placed in a clean tube, followed by another centrifugation at 4,000 rpm for 10 min to collect the Cy5-labeled 5-FU@HFn (Cy5-5-FU@HFn).

Cellular uptake and intracellular localization of 5-FU@HFn

K562 and K562/G01 cells were seeded at a density of 2×10^5 cells per well in a 24-well plate. Cy5-5-FU@HFn was added, and the cells were incubated at 37 °C. Flow cytometry (FCM) was used to analyze the Cy5 fluorescence intensity of the cells. The FCM data were analyzed via FlowJo software. After incubation with Cy5-5-FU@HFn, the CML cells were subsequently harvested, stained with DAPI (Beyotime, China), and observed under a microscope (Leica, Germany). To investigate the intracellular localization of 5-FU@HFn in CML cells, we incubated LysoTracker Green (1:10,000) (Beyotime, China) and Cy5-5-FU@HFn (10.0 μg/mL) with K562 and K562/G01 cells at 37 °C for 1 h. The cells were collected, smeared, fixed with 4% paraformaldehyde at room temperature for 15 min, and stained with DAPI at 37 °C for an additional 15 min. After washing and air drying, the samples were examined via confocal laser scanning microscopy (CLSM) (Leica, Germany).

CD71 blocking assay

K562 and K562/G01 cells were seeded at a density of 2×10^5 cells per well. Each well received 10.0 μg/mL anti-human CD71 polyclonal antibody (Invitrogen, USA) for blocking, with saline serving as the control. After incubation at 37 °C for 30 min, the cells were washed twice with PBS, and the medium was then replaced with RPMI 1640 medium (Gibco, USA). Subsequently, Cy5-5-FU@HFn (10.0 μg/mL) was added for an additional 30-min incubation at 37 °C. The cells were then collected, washed twice, resuspended in PBS for FCM analysis, and stained with DAPI for observation under a microscope (Leica, Germany).

CCK-8 and IC50

For the cytotoxicity analysis, 2,000 cells per well were seeded into a 96-well plate and cultured in 0.1 mL of RPMI-1640 medium (Gibco, USA) supplemented with 10% fetal bovine serum (Gibco, USA). At various time points after the addition of the drug, 10 μL of CCK-8 reagent (BOSTER, China) was added to each well, followed by a 2-h incubation. The absorbance was measured at 450 nm via a microplate reader (BioTek, USA). The IC50 values for 5-FU and 5-FU@HFn in combination with DAC at 48 h were determined from the CCK-8 results via GraphPad Prism 8.0 software.

Colony formation assay

K562 and K562/G01 cells were harvested and seeded into 96-well plates at a density of 50 cells per well to evaluate cell growth and proliferation. The drugs were subsequently added to the wells of each group. After culturing for 7 days, the number of cell colonies was counted, and the colonies were photographed via an inverted microscope (Nikon, Japan).

FCM analysis of dead cells

After drug treatment, the cells from each group were harvested and stained with 5 μL of Annexin V-FITC (Beyotime, China) and 5 μL of PI-PC5.5 (Beyotime, China) within 1 h for death cell analysis via FCM. The percentage of dead cells in each group was analyzed via FlowJo software.

Western blotting

Proteins were resolved via 8–12% SDS–PAGE, transferred to PVDF membranes, and incubated overnight at 4 °C with primary antibodies against GSDME (1:1,000, ab215191, Abcam, UK), PARP (1:2,000, 9532 S, CST, USA), caspase-3 (1:1,000, 9662 S, CST, USA), and β-actin (TA-09, ZSGB-bio, China). A secondary antibody, either goat anti-rabbit (ZSGB-bio, China) or goat anti-mouse IgG-HRP (ZSGB-bio, China), was used at a dilution of 1:3,000. Detection was performed by using an enhanced chemiluminescence (ECL) western blotting substrate.

Caspase-3 activity Inhibition assay

K562 and K562/G01 cells were pretreated with 4 μM DAC for 48 h. The medium was then replaced, and 30 μM 5-FU@HFn along with 10 μM Z-DEVD-FMK (caspase-3 inhibitor) (MCE, USA) was added to the wells, followed by incubation at 37 °C for an additional 48 h. The morphology of the pyroptotic cells was observed and photographed. Total protein was subsequently extracted from the cells in each group, and the expression levels of cleaved caspase-3 and GSDME-N were measured by western blotting.

LDH release assay

K562 or K562/G01 cells were seeded at a density of 4,000 cells per well in 96-well plates. Each drug group consisted of three replicate wells, all of which were incubated for 48 h at 37 °C. The release of LDH was measured in each

well via an LDH Assay Kit (Beyotime, China). The absorbance of each well was measured at 490 nm via a microplate reader (Bio-Tek, USA). The LDH release rate (%) was calculated via the following formula: (Absorbance of drug-treated well – Absorbance of blank well)/(Absorbance of maximum enzyme activity well – Absorbance of blank well) × 100%.

CML mouse model and drug treatment

NOD.Cg-*Prkdc*^{scid}*Il2rg*^{null} (M-NSG) mice (4–5 weeks old) were purchased from the Shanghai Model Organisms Center, Inc. Human hematopoietic stem cells (HSCs) were obtained from Shanghai Milestone Biotechnologies Company. Within 4 h post irradiation (250 cGy X-rays for 30 s), each mouse was injected with 1.0×10^5 HSCs via the tail vein. On day 7, each mouse received an injection of 2×10^6 K562/G01 cells in 100 μL of PBS through the tail vein to establish the CML-HSC-NSG xenograft leukemia model. On days 14 and 16, the mice were injected with 100 μL of 200 μM DAC or 100 μL of the saline control through the tail vein. The mice subsequently received three intravenous drug injections on days 18, 21, and 24; HFn protein (100 μL, 10 mg/mL), 5-FU (100 μL, 0.5 mg/mL), or 5-FU@HFn (100 μL, 10 mg/mL, equivalent for free 5-FU) at each time point. The body weights of the mice were monitored weekly, and the white blood cell (WBC) count in the peripheral blood was assessed. Mouse bone marrow cells were collected, and the percentage of $CD45^+$ cells was determined via FCM with a CD45-PerCP antibody (Raisecare, China). Wright–Giemsa staining, hematoxylin–eosin (HE) staining and immunofluorescence staining were employed to detect CML cell infiltration in the liver, spleen, and bone marrow of the mice. To evaluate the antitumor immunity of each group, we measured the levels of the cytokines IL-1β and IL-6 in the peripheral blood using an IL-1β and IL-6 magnetic particle-based chemiluminescence immunoassay kit (Hotgen, China). Additionally, the percentage of $CD8^+$ T lymphocytes in the peripheral blood was assessed via TBNK reagent (Raisecare, China), the percentage of mature dendritic cells (DCs) in the bone marrow was evaluated via CD80-FITC, CD86-APC, and CD11c-PerCP antibodies (BioLegend, USA), and the protein levels of cleaved caspase-3 and GSDME-N in the bone marrow cells were analyzed by western blotting. All animal procedures employed in the project were approved by the Institutional Animal Care and Use Committee of Chongqing Medical University (IACUC-CQMU-2023-0113).

Distribution and targeting of 5-FU@HFn in vivo

M-NSG mice aged 5–6 weeks were injected with 2.0×10^6 luc-K562/G01 (luciferase-labeled K562/G01) cells via the tail vein to establish a CML-NSG mouse model. On day 14, the mice received an intraperitoneal injection of D-fluorescein potassium salt (3 mg/mouse) (MCE, USA), followed by luminescence imaging via an in vivo imaging system (IVIS, Berthold, Germany) at 560 nm to analyze the distribution of CML cells. The following day, Cy5-5FU@HFn (1 mg/mouse) was injected into the tail vein of the mice. The mice were sacrificed 12-h post injection, and the heart, liver, spleen, lung, kidney, femur, tibia, and fibula were excised. The Cy5 fluorescence intensity of these organs was immediately examined via IVIS to assess the distribution of 5-FU@HFn in the mice. Luminescence and fluorescence images and their intensities were collected and analyzed via IndiGo software.

Safety of 5-FU@HFn in vivo

BALB/c mice, aged 5–6 weeks, were procured from the Experimental Animal Center of Chongqing Medical University. The mice randomly assigned to different drug treat groups and administered via the tail vein for five consecutive days, including a control group (injected with 100 μL of saline), a DAC group (200 μM, 100 μL), a HFn group (10 mg/mL, 100 μL), a 5-FU group (0.5 mg/mL, 100 μL), and a 5-FU@HFn group (10 mg/mL, 100 μL). Following drug administration, the living conditions of the mice were monitored, and fecal samples were collected for occult blood testing (Solarbio, China). Peripheral blood was analyzed via an automatic hematology analyzer (Mindray, China) to assess RBC, WBC, and platelet (PLT) counts. Serum levels of alanine transaminase (ALT), aspartate aminotransferase (AST), blood urea nitrogen (BUN), and creatinine (Cr) were measured via an automatic biochemical analyzer (Siemens, Germany). After the mice were sacrificed, tissues, including heart, liver, spleen, lung, and kidney, were harvested and fixed for subsequent HE staining.

Statistical methods

Statistical analyses were performed via GraphPad Prism 8.0 software, and all the data are presented as the means ± SDs. Group comparisons were assessed via one-way ANOVA, with a p value of less than 0.05 considered to indicate significance.

Other methods

For detailed procedures of other methods, please refer to Additional File 1 in the Supplementary Materials.

Results

Preparation and characteristics of 5-FU@HFn

The 5-FU@HFn was successfully synthesized via the high-temperature method, which is illustrated in Fig. 1A. The quantity of 5-FU loading in HFn was quantified indirectly by measuring its concentration in the ultrafiltrate via HPLC at 265 nm, the standard curve of 5-FU was

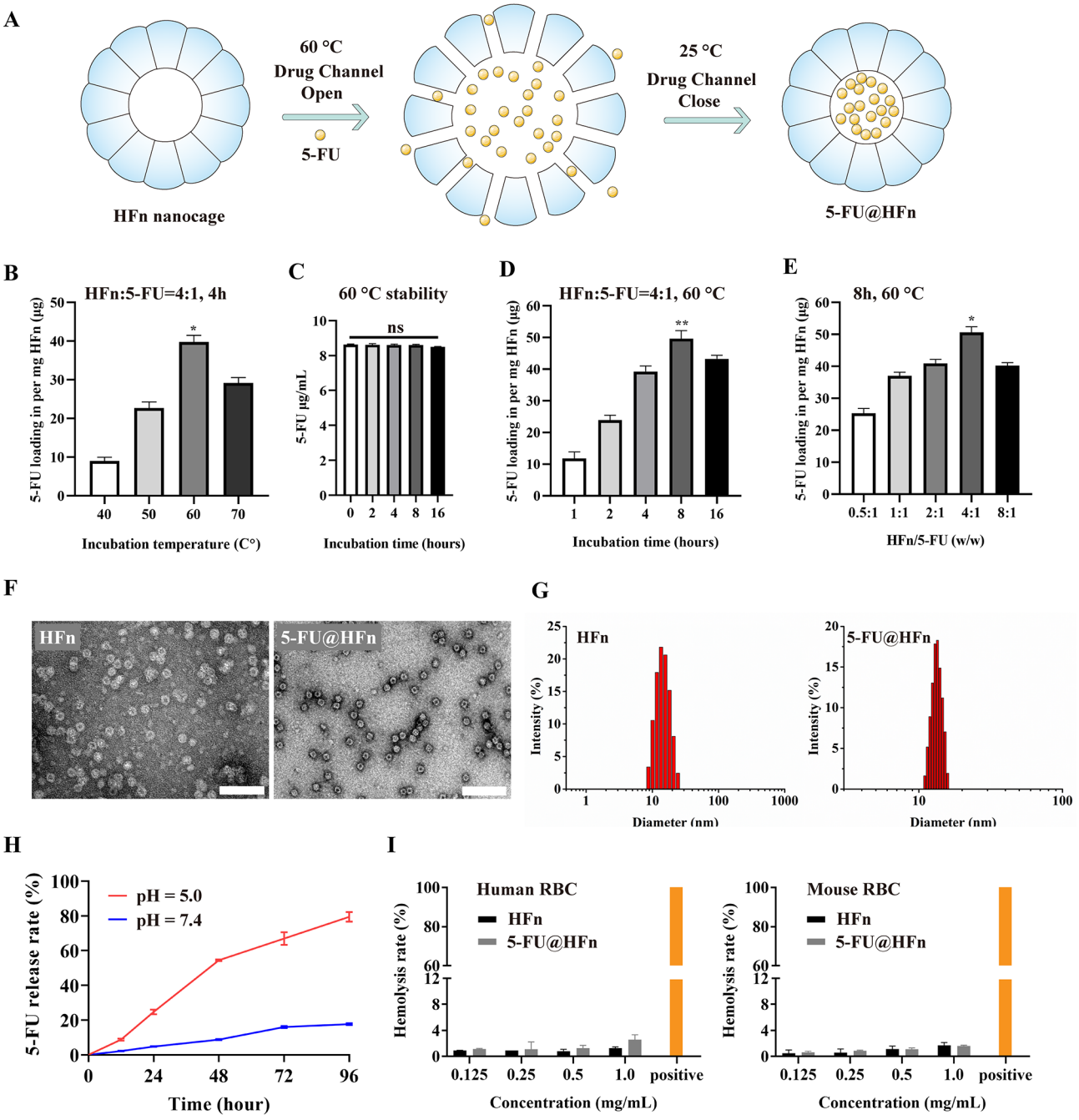

Fig. 1 Preparation and characteristics of 5-FU@HFn. (**A**) Schematic illustration of the process for loading 5-FU into HFn nanocage via a high-temperature method. (**B**) The loading efficiency (5-FU in per mg HFn) of 5-FU was evaluated at different temperature. (**C**) Stability assessment of 5-FU at 60 °C. (**D**) The loading efficiency was investigated at different incubation time. (**E**) The loading efficiency was examined at different HFn/5-FU mass ratios. (**F**) Transmission electron microscopy (TEM) images of HFn and 5-FU@HFn. Scale bar: 50 nm. (**G**) Dynamic light scattering (DLS) was used to analyze the diameters of HFn and 5-FU@HFn. (**H**) The release rate of 5-FU from 5-FU@HFn was evaluated under acidic (pH 5.0) and neutral (pH 7.4) conditions. (**I**) Hemolysis rates of HFn and 5-FU@HFn were analyzed at various concentrations in human and mouse red blood cells (RBCs). The data are presented as the means ± SDs; * $P < 0.05$, ** $P < 0.01$, ns: not significant

shown in Fig. S1. The optimal loading conditions for preparing 5-FU@HFn was an HFn/5-FU mass ratio of 4:1 and an 8 h incubation at 60 °C (Fig. 1B–E). The results indicated that each milligram of HFn loaded approximately 50.62 ± 1.17 μg of 5-FU (Table S1). The structural integrity of both HFn and 5-FU@HFn was confirmed via TEM and DLS. The TEM results revealed that 5-FU@HFn retained a monodispersed core-shell spherical structure (Fig. 1F), indicating that the loading of 5-FU did not disrupt the nanocage structure of HFn. DLS analysis

further demonstrated the uniformity of the nanoparticles, with diameters of approximately 13.61 ± 0.95 nm and 13.86 ± 0.44 nm for HFn and 5-FU@HFn, respectively (Fig. 1G). To investigate the release rate, 5-FU@HFn was diluted in PBS at various pH values and gently shaken to simulate the cellular environment. The results demonstrated a significantly greater release rate of 5-FU (79.45 ± 2.77% in 96 h) in an acidic environment than in a neutral environment (17.75 ± 0.52% in 96 h) (Fig. 1H and Table S1). These findings suggest that 5-FU@HFn may be particularly effective for targeted drug delivery to acidic tumor microenvironments. A hemolysis assay was performed to evaluate the blood compatibility of 5-FU@HFn. As shown in Fig. 1I, both HFn and 5-FU@HFn at certain concentrations (0.125–1.0 mg/mL) resulted in low hemolysis rates, indicating good potential for in vivo applications.

Cellular uptake and localization of 5-FU@HFn

The cellular uptake of 5-FU@HFn in K562 and K562/G01 cells was examined via FCM and CLSM. To visualize the intracellular distribution of 5-FU@HFn, Cy5 was conjugated to 5-FU@HFn because of its strong red fluorescence intensity. FCM analysis (Fig. 2A) revealed that the cellular uptake of 5-FU@HFn was time-dependent, beginning as early as 0.25 h and gradually increasing from 0.5 h to 4 h. Furthermore, the intracellular uptake of 5-FU@HFn was dose-dependent, with higher doses resulting in increased cell fluorescence intensity (Fig. 2B). CLSM imaging (Fig. 2C) further confirmed the uptake of 5-FU@HFn. To investigate the intracellular localization of 5-FU@HFn, we cultured CML cells with LysoTracker Green and Cy5-5-FU@HFn. As shown in Fig. 2D, a distinct colocalization of red and green fluorescence was observed within the cells following coincubation, indicating that most of the 5-FU@HFn localized in the lysosomes upon intracellular uptake.

To further elucidate the mechanism of 5-FU@HFn uptake by CML cells, we analyzed the expression of the CD71 on CML cells and assessed their capacity for the cellular uptake of 5-FU@HFn after blocking the CD71 epitopes with a CD71 polyclonal antibody. FCM analysis revealed high expression of CD71 on the surface of both K562 and K562/G01 cells (Fig. 2E). Additionally, a notable decrease in the uptake of 5-FU@HFn by CML cells was observed upon CD71 blockade (Fig. 2F). CLSM further confirmed a significant reduction in the uptake of 5-FU@HFn by CML cells following CD71 blockade (Fig. 2F). These findings suggest that 5-FU@HFn can potentially enable targeted drug delivery to CML cells via CD71-mediated uptake, which may enhance the efficacy of 5-FU in treating CML.

DAC combined with 5-FU@HFn suppresses proliferation and induces death in CML cells

Previous experiments confirmed that a low dose of DAC (4 μM) significantly upregulates GSDME expression in CML cells (K562 and K562/G01), likely due to histone lysine demethylase (KDM)-mediated demethylation (Fig. S2A–H). To assess the therapeutic potential of DAC (4 μM) in combination with 5-FU or 5-FU@HFn, we performed a CCK-8 assay to evaluate CML cell proliferation inhibition. The results demonstrated that DAC + 5-FU or DAC + 5-FU@HFn effectively suppressed CML cell proliferation, with 5-FU@HFn exhibiting superior efficacy compared to 5-FU at equivalent concentrations (Fig. S3A–D). IC50 analysis at 48 h revealed: in K562 cells, the IC50 of 5-FU@HFn was 32.70 ± 2.22 μM, approximately 2.5-fold lower than that of 5-FU (83.30 ± 4.22 μM) (Fig. 3A); in K562/G01 cells, the IC50 of 5-FU@HFn was 22.25 ± 1.20 μM, indicating a 3.6-fold lower than that of 5-FU (79.03 ± 2.80 μM) (Fig. 3B).

To further assess the suppression of cell proliferation, we conducted a colony formation assay. The results revealed a significant reduction in both the number and size of cell clones in the 5-FU@HFn and DAC + 5-FU@HFn groups compared to the other treatment groups (Fig. 3C, E). Notably, while 5-FU and DAC + 5-FU also inhibited colony formation, the most pronounced effect was observed in the DAC + 5-FU@HFn group (Fig. 3C, E). To investigate the death cells, we performed FCM to assess the percentage of dead (apoptotic/pyroptotic) cells in each treatment group. The DAC + 5-FU@HFn group exhibited the highest percentage of dead CML cells, with a notable increase also observed in the 5-FU@HFn, 5-FU, and DAC + 5-FU groups (Fig. 3D, F). In contrast, no significant difference in cell death was observed in the control groups (Fig. 3D, F). Collectively, these findings indicate that DAC + 5-FU@HFn potently inhibits CML cell proliferation and effectively induces cell death, most likely via pyroptosis.

DAC combined with 5-FU@HFn induced pyroptosis in CML cells

To confirm that DAC + 5-FU@HFn effectively induces pyroptosis in CML cells, we analyzed cell morphology, cytokine secretion, and GSDME cleavage following treatment. Microscopic observations revealed a significant number of pyroptotic cells in the DAC + 5-FU@HFn group, characterized by cell swelling, membrane perforation, and plasma membrane bubble formation (Fig. 4A). In contrast, fewer pyroptotic cells were observed in the DAC + 5-FU group, while none were detected in the other groups. TEM further confirmed pyroptotic features in DAC + 5-FU@HFn-treated cells, including bubble-like protrusions, pore formation, loss of membrane integrity, and intracellular content release (Fig. 4B). Western

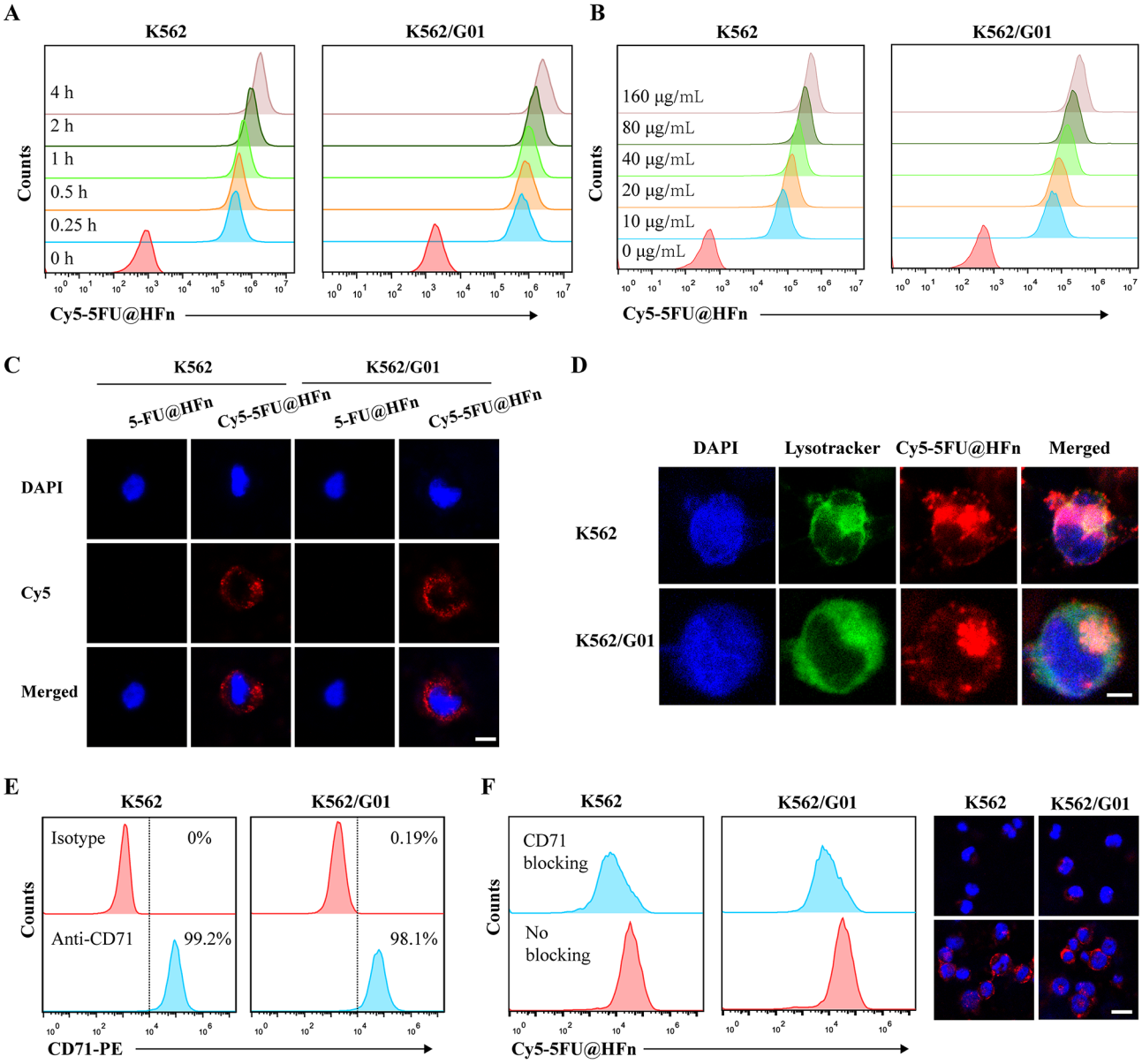

Fig. 2 Cellular uptake and localization of 5-FU@HFn. (A) Flow cytometry (FCM) was used to analyze the time-dependent uptake of Cy5-5-FU@HFn at a dose of 40 μg/mL in K562 and K562/G01 cells. (B) FCM analysis of the intercellular uptake of Cy5-5-FU@HFn in K562 and K562/G01 cells at different doses. (C) Confocal laser scanning microscopy (CLSM) images of K562 and K562/G01 cells after incubation with Cy5-5-FU@HFn. Scale bar: 10 μm. (D) CLSM images of the intracellular localization of Cy5-5-FU@HFn in K562 and K562/G01 cells. Scale bar: 5 μm. 5-FU@HFn (Cy5; red), LysoTracker (FITC; green), and Nuclei (4′,6-diamidino-2-phenylindole (DAPI); blue). (E) FCM analysis of CD71 expression in K562 and K562/G01 cells. Isotype: PE-Mouse IgG2a,k. (F) FCM and CLSM were used to analyze the intercellular uptake of Cy5-5-FU@HFn in CML cells pretreated with an anti-CD71 antibody. Scale bar: 10 μm

blotting revealed the presence of cleaved caspase-3 and cleaved PARP in the DAC + 5-FU@HFn group (Fig. 4C), indicating caspase-3 activation. Importantly, significant GSDME-N protein expression was detected in this group (Fig. 4C), confirming GSDME-mediated pyroptosis in CML cells. These findings were further validated by the LDH release assay, which showed substantial LDH release in the DAC + 5-FU@HFn group (Fig. 4D), indicating membrane rupture and pyroptotic cell death. Additionally, HMGB-1 and IL-1β levels were significantly elevated (Fig. 4D), suggesting that DAC + 5-FU@HFn not only induces pyroptosis but also stimulates an antitumor immune response.

To further elucidate the role of caspase-3 in GSDME-mediated pyroptosis, we performed a caspase-3 inhibition assay. When CML cells were co-treated with the caspase-3 inhibitor Z-DEVD-FMK, they exhibited robust growth without morphological features of pyroptosis under microscopic examination (Fig. 4E). Western blotting confirmed the absence of cleaved caspase-3 and

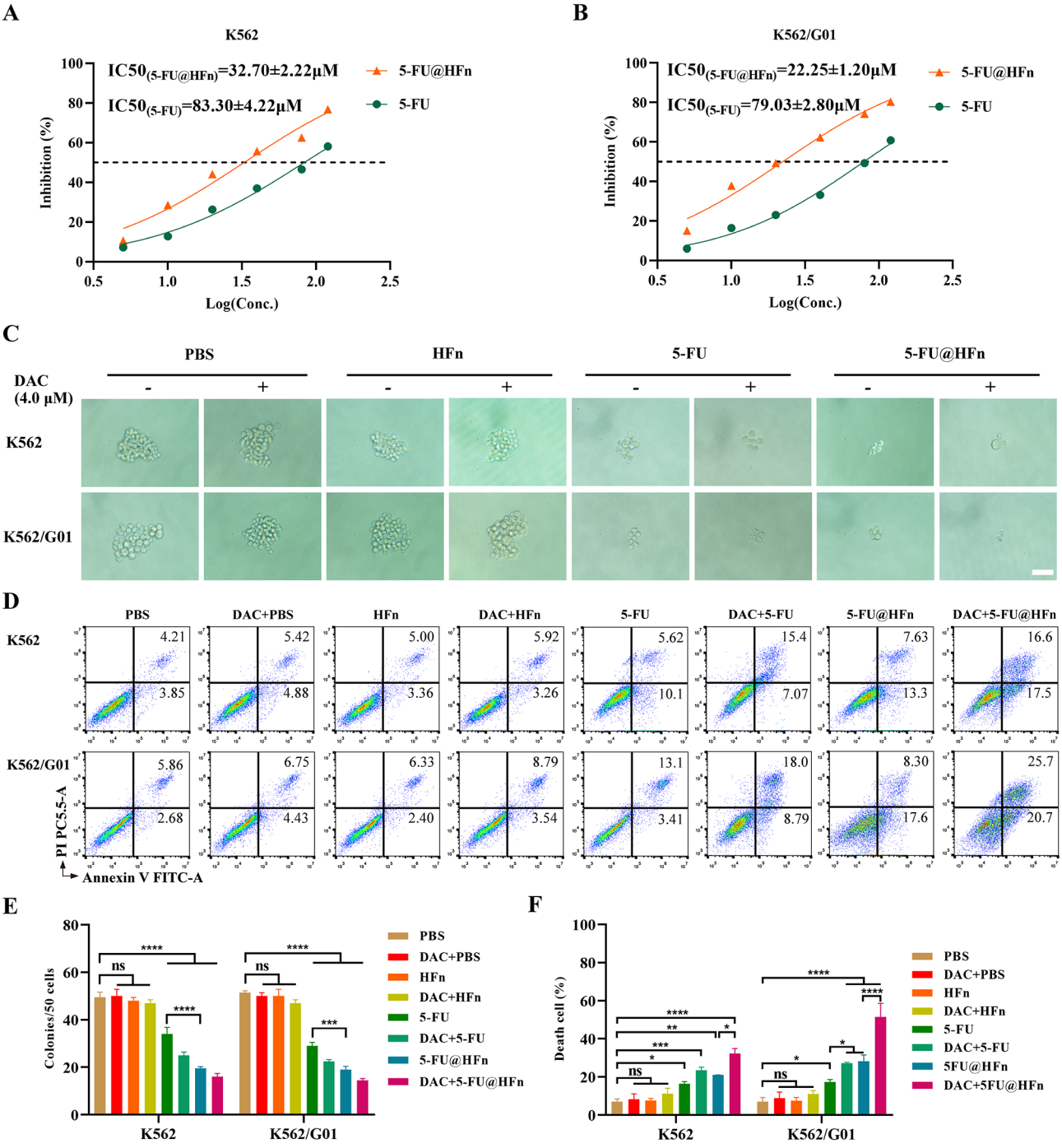

Fig. 3 Decitabine (DAC) combined with 5-FU@HFn affects CML cells. (**A**) The IC50 values of 5-FU and 5-FU@HFn in K562 cells were determined via a CCK-8 assay at 48 h. (**B**) The IC50 values of 5-FU and 5-FU@HFn in K562/G01 cells were determined via a CCK-8 assay at 48 h. (**C**, **E**) Colony formation assay for K562 and K562/G01 cells, which were observed and counted under a microscope. Scale bar: 50 μm. (**D**, **F**) Flow cytometry (FCM) analysis was performed to determine the death rate of CML cells. The data are presented as the means ± SDs. * $P < 0.05$, ** $P < 0.01$, *** $P < 0.001$, **** $P < 0.0001$, ns: not significant

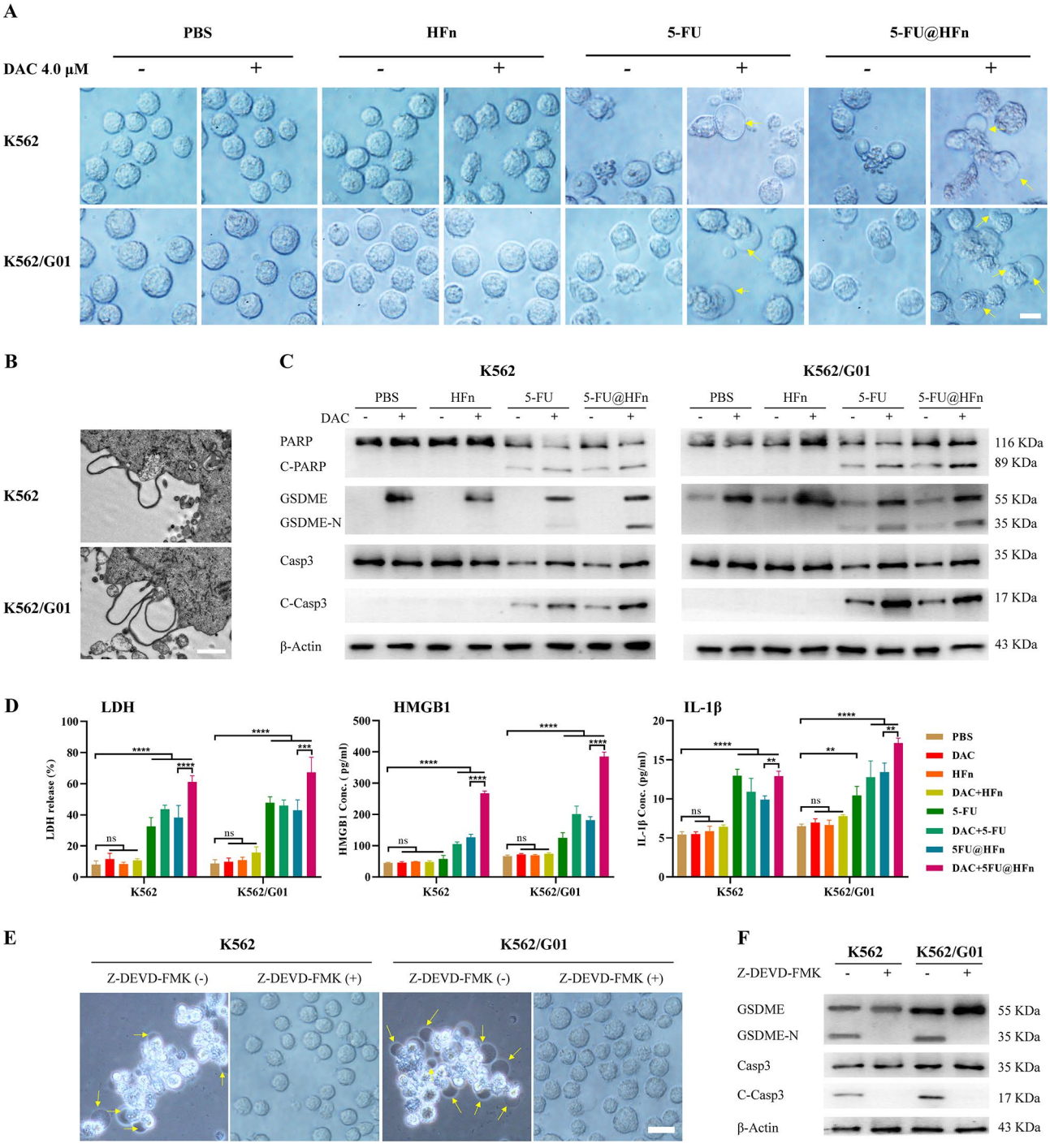

Fig. 4 Decitabine (DAC) combined with 5-FU@HFn to induce CML cell pyroptosis. (**A**) Morphological observations of CML cells in each drug treatment group were conducted via microscopy. The yellow arrow indicates pyroptotic cells. Scale bar: 10 μm. (**B**) Transmission electron microscopy (TEM) was used to observe membrane changes in pyroptotic cells in the DAC + 5-FU@HFn treatment group. Scale bar: 1 μm. (**C**) Western blot assays were utilized to assess cleaved PARP (C-PARP), cleaved caspase-3 (C-Casp3), and GSDME-N protein expression levels. (**D**) Lactate dehydrogenase (LDH) release rates (%), high mobility group box 1 (HMGB1) levels (gp/mL), and IL-1β levels (pg/mL) in each group were analyzed. (**E**) After inhibition of caspase-3 activity by Z-DEVD-FMK in the DAC + 5-FU@HFn group, pyroptotic cells were observed under a microscope, as indicated by the yellow arrow. Scale bar: 10 μm. (**F**) Western blot analysis was performed to assess the expression levels of C-Casp3 and GSDME-N in the DAC + 5-FU@HFn group treated with Z-DEVD-FMK. All the data are presented as the means ± SDs. ** $P < 0.01$, *** $P < 0.001$, **** $P < 0.0001$, ns: not significant

GSDME-N proteins in these cells (Fig. 4F), demonstrating that caspase-3 activity is required for GSDME cleavage and pyroptosis induction.

DAC + 5-FU@HFn impaired oncogenesis in vivo

To evaluate the in vivo efficacy of DAC + 5-FU@HFn in leukemia suppression and immune-mediated antitumor activity, we established a humanized HSC-NSG mouse model with a functional immune system. We then injected K562/G01 cells intravenously to generate a CML-HSC-NSG mouse model. One week of post-injection, CML-HSC-NSG mice received sequential DAC and 5-FU@HFn treatments via the tail vein (Fig. 5A). Body weights and peripheral blood WBC counts were monitored weekly. The DAC + 5-FU@HFn group exhibited only a slight weight reduction, whereas mice in other groups experienced significant weight loss starting from day 30 (Fig. 5B). As expected, the WBC count in the DAC + 5-FU@HFn group was significantly lower than in the control groups (Fig. 5C).

To assess leukemia progression, we analyzed the percentage of human $CD45^+$ cells in bone marrow via FCM. The DAC + 5-FU@HFn group exhibited a notably lower proportion of $CD45^+$ cells compared to other groups (Fig. 5D). Additionally, liver and spleen weights were measured, revealing that mice in the DAC + 5-FU@HFn group did not develop hepatosplenomegaly, unlike those in the other groups (Fig. 5E). Wright-Giemsa and HE staining of the liver, spleen, and bone marrow demonstrated an absence of leukemic cell infiltration in the DAC + 5-FU@HFn group, whereas significant infiltration was observed in other groups (Fig. 5F and Fig. S4). Furthermore, immunofluorescence analysis confirmed markedly lower BCR/ABL protein expression in the liver, spleen, and bone marrow of DAC + 5-FU@HFn-treated mice compared to other groups (Fig. 5G). These findings collectively demonstrate that DAC + 5-FU@HFn therapy effectively suppresses leukemia progression, reduces the oncogenic potential of K562/G01 cells, and holds significant therapeutic promise for CML.

DAC + 5-FU@HFn induced pyroptosis and activated antitumor immunity in CML mice

Next, we investigated the impact of DAC + 5-FU@HFn treatment on GSDME-mediated pyroptosis in CML cells and its role in enhancing antitumor immunity in vivo. Western blot analysis of bone marrow cells revealed a distinct GSDME-N protein band in the DAC + 5-FU@HFn group, confirming the induction of pyroptosis, which was absent in the control groups (Fig. 6A). Additionally, levels of IL-1β and IL-6 in peripheral blood were highest in the DAC + 5-FU@HFn-treated group (Fig. 6B, C), indicating a robust inflammatory response crucial for T-cell proliferation and activation. FCM analysis of peripheral blood showed a marked increase in T lymphocytes and a decrease in $CD45^+$ leukemia cells in the DAC + 5-FU@HFn group (Fig. S5), suggesting effective immune activation and leukemia cell clearance. Specifically, the percentage of $CD8^+$ T lymphocytes was significantly elevated (Fig. 6D, F), highlighting the activation of tumor-specific immune responses. Furthermore, FCM analysis of bone marrow cells demonstrated a significant increase in mature dendritic cells (DCs) (Fig. 6E, G), which are critical for naïve T-cell activation and $CD8^+$ T-cell-driven immune responses. Finally, Kaplan-Meier survival analysis revealed that mice treated with DAC + 5-FU@HFn exhibited a significantly prolonged survival time compared to control groups (Fig. 6H). These findings indicate that DAC + 5-FU@HFn therapy effectively induces pyroptosis in CML cells while simultaneously triggering a potent, tumor-specific immune response in vivo.

Targeting and biosafety of 5-FU@HFn in vivo

Bioluminescence imaging of the CML-NSG model established with luc-K562/G01 cells revealed that leukemic cells primarily infiltrated the liver, spleen, and bone marrow (Fig. 7A). To assess the in vivo distribution of 5-FU@HFn, Cy5-labeled 5-FU@HFn was administered via the tail vein, followed by fluorescence imaging of major organs. Strong fluorescence signals were detected in the livers and kidneys of both CML-NSG and control mice (Fig. 7B), confirming that 5-FU@HFn is primarily metabolized in these organs. Notably, in CML-NSG mice, fluorescence was also observed in the spleen and bone marrow (Fig. 7B), indicating effective targeting of CML cells in vivo.

To evaluate biosafety, 5-FU@HFn and other treatments were administered via the tail vein to BALB/c mice, followed by assessments of fecal occult blood (FOB) (Fig. 7C), complete blood count (RBC, WBC, PLT) (Fig. 7D–F), liver function (ALT, AST) (Fig. S6A, B), kidney function (BUN, Cr) (Fig. S6C, D), and histopathological analysis (HE staining) of major organs (Fig. S6E). No significant differences were observed between the 5-FU@HFn and control groups, confirming its excellent in vivo safety. Additionally, mice treated with HFn or DAC alone also exhibited favorable safety. In contrast, 5-FU-treated mice displayed notable side effects, including gastrointestinal bleeding (positive FOB) (Fig. 7C) and reduced platelet counts (Fig. 7F). These findings demonstrate that 5-FU@HFn effectively mitigates the side effects of 5-FU, enhancing its clinical translational potential.

Discussion

CML is a hematopoietic stem cell disorder driven by the t(9;22)(q34; q11) translocation, which results in the formation of the BCR/ABL fusion gene [2]. This fusion gene encodes the BCR/ABL oncoprotein, which possesses

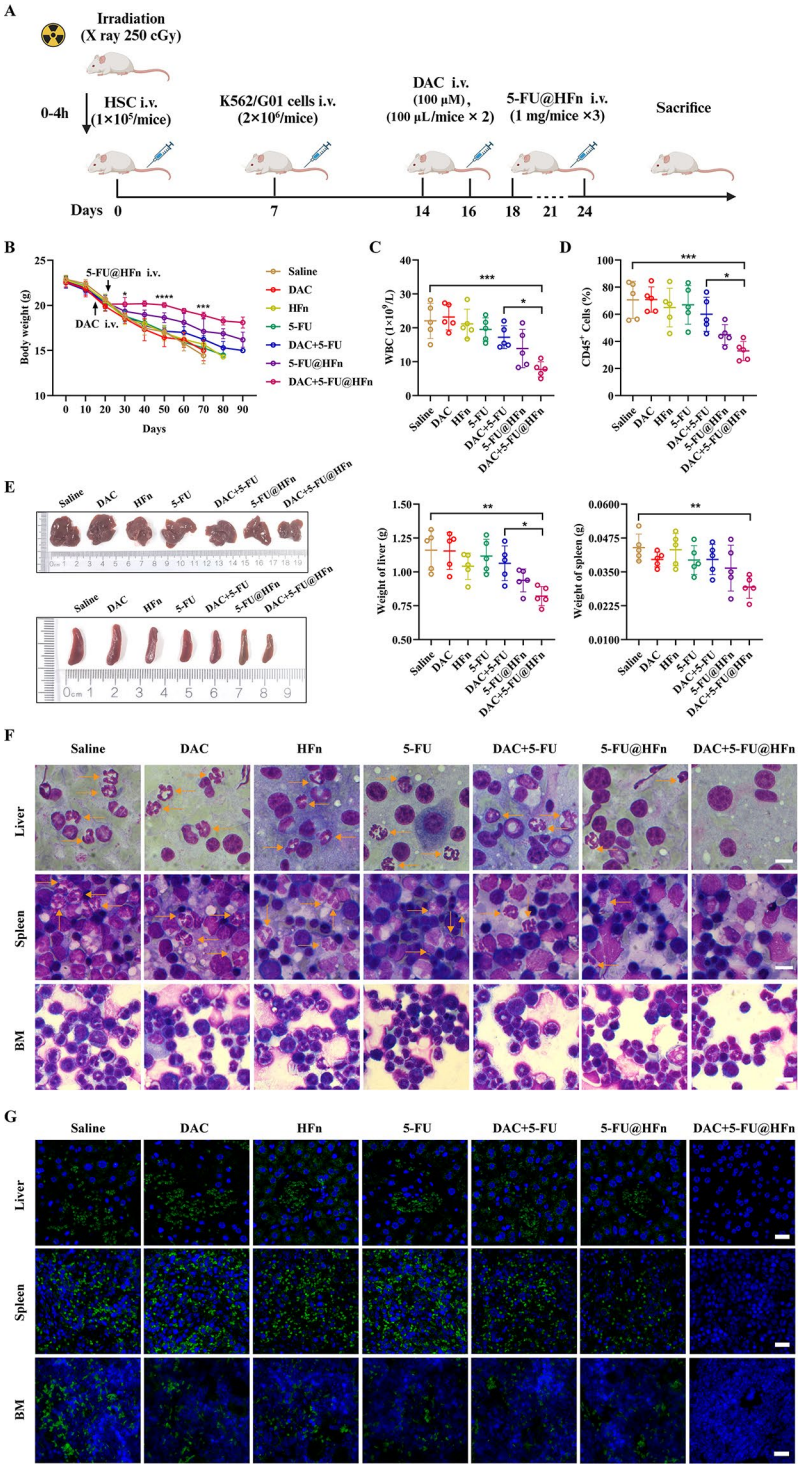

Fig. 5 DAC + 5-FU@HFn impaired the oncogenesis of CML cells in vivo. (**A**) A CML-HSC-NSG mouse model was established and subjected to a designated treatment regimen. (**B**) The body weights of the mice were recorded for 90 days. (**C**) The maximum white blood cell (WBC) counts in the peripheral blood of the mice were measured. (**D**) The percentage of $CD45^+$ cells in the bone marrow of the mice was detected via flow cytometry (FCM). (**E**) The weights and sizes of the liver and spleen were measured in CML mice. (**F**) Liver, spleen, and bone marrow (BM) samples from CML mice were examined via Wright–Giemsa staining. The infiltrating leukemic cells are indicated by arrows. Scale bar: 10 μm. (**G**) Immunofluorescence staining was performed to analyze the protein expression of BCR/ABL in the liver, spleen, and bone marrow of CML mice. Scale bar: 20 μm. All the data are presented as the means ± SDs. * $P < 0.05$, ** $P < 0.01$, *** $P < 0.001$, **** $P < 0.0001$

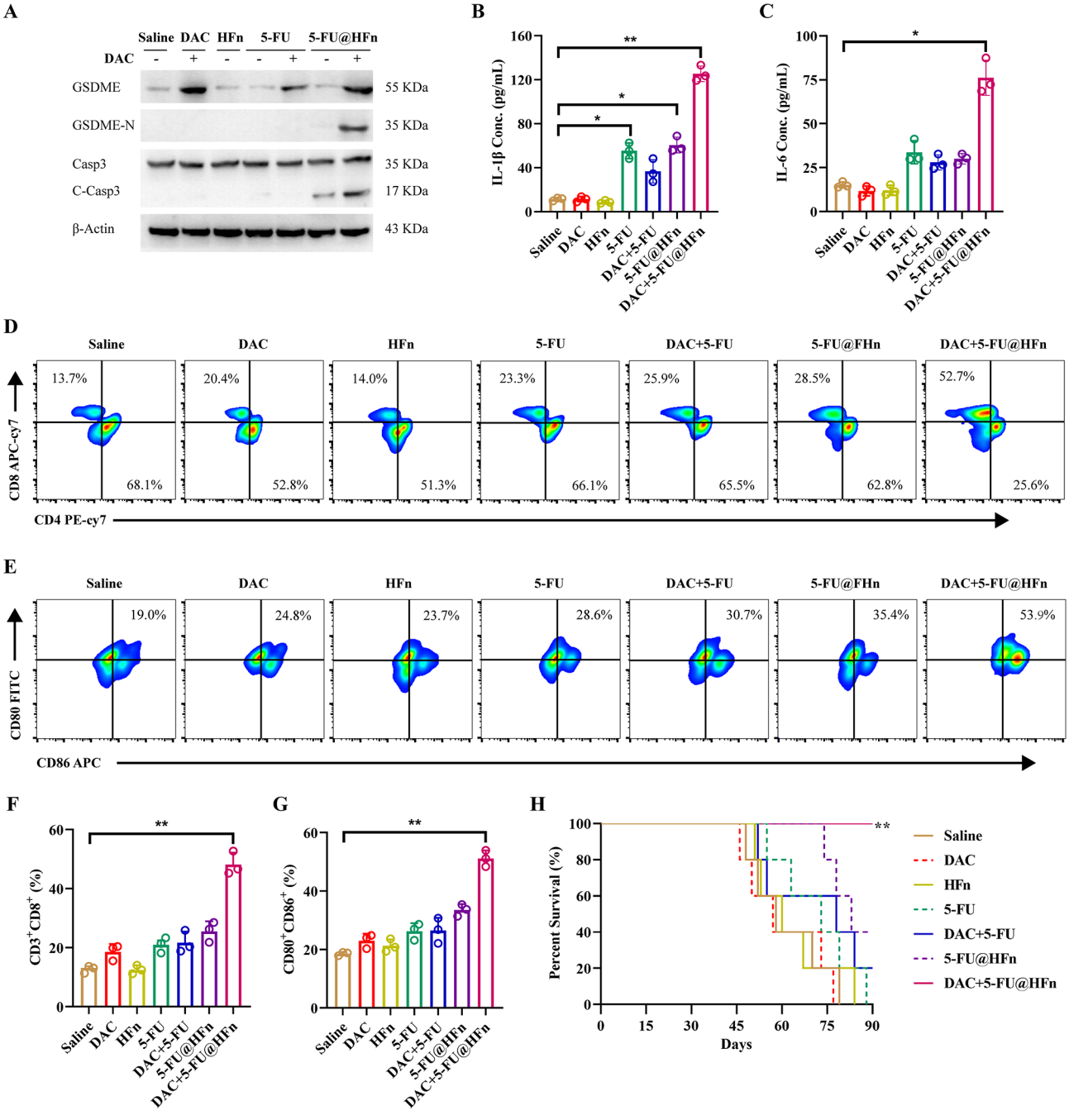

Fig. 6 DAC + 5-FU@HFn induced pyroptosis and activated antitumor immunity in CML mice. (**A**) Western blot analysis of GSDME-N and cleaved caspase-3 (C-Casp3) protein expression in the bone marrow cells of CML mice. (**B**) IL-1β (pg/mL) and (**C**) IL-6 (pg/mL) levels in the blood of CML mice in different groups were measured. (**D**) (**F**) The percentages of $CD8^+$ T lymphocyte subsets in the peripheral blood of CML mice were analyzed by flow cytometry (FCM). (**E**) (**G**) The percentage of mature dendritic cells (DCs) analyzed by FCM in CML mouse bone marrow cells. (**H**) Kaplan–Meier survival curves for CML mice. All the data are presented as the means ± SDs. * $P < 0.05$, ** $P < 0.01$

aberrant tyrosine kinase activity and plays a pivotal role in leukemogenesis [33]. Targeting or eradicating the tyrosine kinase activity of BCR/ABL is the primary therapeutic approach for CML due to its substantial contribution to disease progression. The advent of tyrosine kinase inhibitors (TKIs), such as imatinib, has transformed CML treatment, particularly in the chronic phase. However, resistance and intolerance remain significant challenges [34]. Mutations in the BCR/ABL kinase domain, especially the T315I mutation, confer resistance to both first- and second-generation TKIs [35]. While third-generation TKIs demonstrate efficacy against T315I-mutant

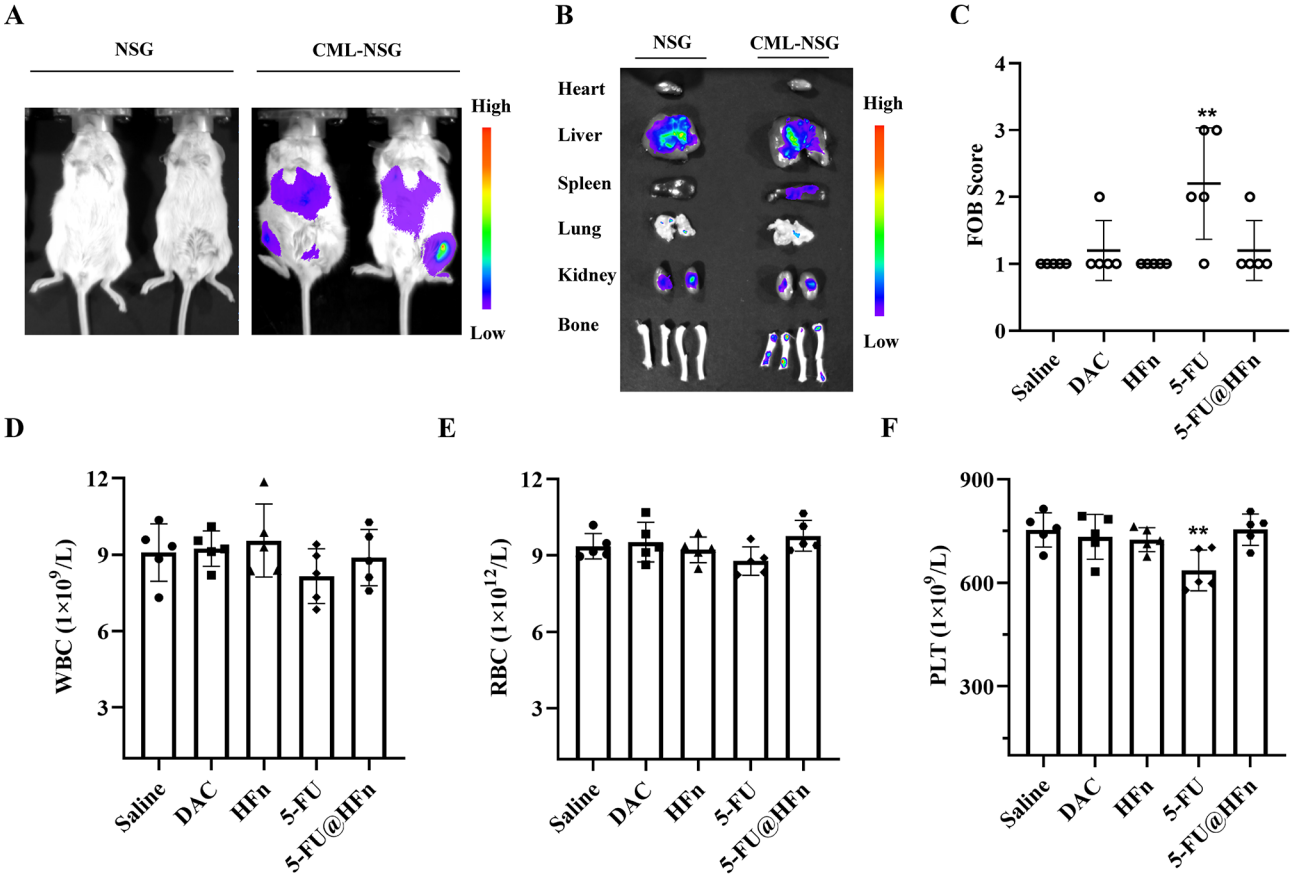

Fig. 7 Distribution and biosafety of 5-FU@HFn in vivo. (**A**) Bioluminescence imaging revealed CML cell infiltration in the CML-NSG mouse model established with luc-K562/G01 cells. (**B**) Fluorescence images of major organs anatomized from CML-NSG mice 12 h after intravenous injection of Cy5-5-FU@HFn. (**C**) Fecal occult blood (FOB) scores were calculated from the FOB test results of BALB/c mice. (**D**) White blood cell (WBC), (**E**) red blood cell (RBC), and (**F**) platelet (PLT) counts in the peripheral blood of BALB/c mice were recorded after treatment with drugs. All the data are presented as the means ± SDs. ** $P < 0.01$

CML, they are often associated with increased toxicity and a higher incidence of adverse effects [35]. These limitations underscore the urgent need for novel therapeutic strategies to overcome resistance and improve clinical outcomes.

In this study, we presented a novel therapeutic strategy combining 5-FU@HFn, a nanodrug delivery system, with low-dose decitabine (DAC) to induce GSDME-mediated pyroptosis and activate specific antitumor immunity in CML cells. The 5-FU@HFn system demonstrated excellent targeting specificity and biosafety, effectively delivering 5-FU to CML cells while sparing normal tissues (Figs. 2 and 7). Compared to conventional pH- or urea gradient-based loading techniques, the high-temperature (60 °C) assembly method [27, 32] improved drug-loading efficiency and simplified the preparation process. This targeted approach not only enhanced the therapeutic effects of 5-FU by inducing pyroptosis (Figs. 4 and 6) but also significantly reduced systemic toxicity, including gastrointestinal bleeding and thrombocytopenia, as observed in vivo (Fig. 7C, F). The selectivity of 5-FU@HFn is attributed to the high expression of CD71 in CML cells, which serves as a natural receptor for HFn, facilitating precise drug delivery [26, 30]. Additionally, the HFn nanocage offers advantages over synthetic nanocarriers, including biocompatibility, low toxicity, and enhanced immune tolerance [36, 37]. Collectively, these findings highlight the translational potential of the 5-FU@HFn nanodrug delivery system for CML therapy.

Our results further revealed that combining 5-FU@HFn with low-dose DAC effectively induced GSDME-mediated pyroptosis and activated antitumor immune responses. 5-FU@HFn triggered caspase-3 activation, a key mediator of apoptosis [38], leading to GSDME cleavage [39]. Low-dose DAC upregulated GSDME expression, facilitating its cleavage into GSDME-N fragments, which induced pyroptosis [40, 41]. This approach repurposes 5-FU, utilizing its pyroptosis-inducing potential in conjunction with epigenetic modulation via DAC, introducing a novel therapeutic application for this widely used chemotherapeutic agent. In vitro experiments confirmed that DAC + 5-FU@HFn effectively converted

caspase-3-dependent apoptosis into pyroptosis in both TKI-sensitive and TKI-resistant CML cells (Figs. 3 and 4). In vivo studies further validated that this combination suppressed leukemogenesis by inducing pyroptosis and stimulating antitumor immune responses (Figs. 5 and 6). Unlike traditional TKI therapies [42, 43], this approach does not require long-term drug administration, exhibits minimal side effects, and is well-tolerated. Most importantly, short-term combination treatment activated antitumor immune cells, including $CD8^+$ T cells and dendritic cells (DCs), which facilitated the rapid clearance of residual leukemia cells. Unlike adoptive immunotherapy [44, 45], this strategy directly activates endogenous antitumor immune cells without requiring ex vivo cell manipulation and reinfusion, potentially reducing the risk of cytokine storms and infections. These findings support DAC + 5-FU@HFn as a simple, safe, and effective therapeutic strategy for CML patients resistant or intolerant to TKIs.

Despite these promising results, several limitations remain. First, the release kinetics and pharmacokinetics of 5-FU@HFn in vivo require further characterization to optimize drug exposure and minimize off-target effects. Second, the optimal drug concentration and potential long-term toxicity need to be carefully evaluated. Third, our study utilized cell line-derived xenograft (CDX) models, which may not fully recapitulate the immune microenvironment and hematopoietic conditions in CML patients. To address this limitation, future research will employ patient-derived xenograft (PDX) models, generated from primary bone marrow cells of newly diagnosed CML patients, to provide a more clinically relevant assessment of the DAC + 5-FU@HFn combination therapy.

Conclusions

This study provides the first evidence that the combination of 5-FU@HFn nanoparticles and low-dose DAC induces caspase-3/GSDME-mediated pyroptosis in CML cells, demonstrating potent antitumor efficacy in vitro and in vivo. This nanodrug delivery strategy represents a safe, effective, and innovative therapeutic approach, particularly for patients with TKI-resistant or TKI-intolerant. By inducing pyroptosis and activating antitumor immunity, this strategy offers a compelling alternative to conventional TKIs, potentially improving clinical outcomes for CML patients.

Abbreviations

TKIs	Tyrosine kinase inhibitors
CML	Chronic myeloid leukemia
5-FU	5-Fluorouracil
DAC	Decitabine
NPs	Nanoparticles
HFn	Heavy chain ferritin
TEM	Transmission electron microscopy
DLS	Dynamic light scattering
FCM	Flow cytometry
CLSM	Confocal laser scanning microscopy
HSCs	Hematopoietic stem cells
HSCT	Hematopoietic stem cell transplantation
GVHD	Graft versus host disease
LDH	Lactate dehydrogenase
IL-1β	Interleukin-1β
IL-6	Interleukin-6
HMGB-1	High mobility group box 1
GSDME	Gasdermin E
DNMT	DNA methyltransferase
CD71	Transferrin receptor 1
HPLC	High-performance liquid chromatography
HE	Hematoxylin-eosin
DCs	Dendritic cells
RBC	Red blood cell
WBC	White blood cell
PLT	Platelet
ALT	Alanine transaminase
AST	Aspartate aminotransferase
BUN	Blood urea nitrogen
Cr	Creatinine
FOB	Fecal occult blood

Supplementary Information

The online version contains supplementary material available at https://doi.org/10.1186/s12951-025-03335-9.

Supplementary Material 1

Acknowledgements

Not applicable.

Author contributions

ZWY and WLF conceived and designed the experiment. ZWY, GYJ and YY completed the experiment and wrote the manuscript. YY, QL and YXH analyzed the results, and revised the manuscript. WYZ and LJT completed the in vivo experiment. KLF and WLF supervised the whole experiment and critically revised the manuscript. All authors read and approved the final manuscript.

Funding

This work was funded by the National Natural Science Foundation of China (No. 81772255; No. 32201167), the Shandong Provincial Natural Science Foundation (No. ZR2023QH062).

Data availability

The data generated during the current study are available from the corresponding author on reasonable request.

Declarations

Ethics approval and consent to participate

All animal experiments were in accordance with the National Institutes of Health guide for the care and use of Laboratory animals (NIH Publications No.8023, revised 1978). All animal procedures employed in the project were approved by the Institutional Animal Care and Use Committee of Chongqing Medical University (IACUC-CQMU-2023-0113).

Consent for publication

Not applicable.

Competing interests

The authors declare no competing interests.

Author details
[1]Department of Clinical Hematology, School of Laboratory Medicine, Key Laboratory of Clinical Laboratory Diagnostics (Ministry of Education), Chongqing Medical University, Chongqing 400016, China
[2]Department of Clinical Laboratory, Chongqing Hospital of Traditional Chinese Medicine, Chongqing 400021, China
[3]Department of Clinical Laboratory, Shandong Provincial Hospital Affiliated to Shandong First Medical University, Jinan, Shandong 250021, China
[4]Department of Respiratory and Critical Care Medicine, The First Affiliated Hospital of Chongqing Medical University, Chongqing 400016, China
[5]Nanozyme Laboratory in Zhongyuan, Henan Academy of Innovations in Medical Science, Zhengzhou, Henan 451163, China
[6]Key Laboratory of Biomacromolecules (CAS), CAS Center for Excellence in Biomacromolecules, Institute of Biophysics, CAS Engineering Laboratory for Nanozyme, Chinese Academy of Sciences, Beijing 100101, China

Received: 1 January 2025 / Accepted: 16 March 2025
Published online: 28 March 2025

References

1. Bartram CR, de Klein A, Hagemeijer A, van Agthoven T, van Geurts A, Bootsma D, et al. Translocation of c-ab1 oncogene correlates with the presence of a Philadelphia chromosome in chronic myelocytic leukaemia. Nature. 1983;306(5940):277–80.
2. Ren R. Mechanisms of BCR-ABL in the pathogenesis of chronic myelogenous leukaemia. Nat Rev Cancer. 2005;5(3):172–83.
3. Shah NP, Bhatia R, Altman JK, Amaya M, Begna KH, Berman E, et al. Chronic myeloid leukemia, version 2.2024, NCCN clinical practice guidelines in oncology. J Natl Compr Canc Netw. 2024;22(1):43–69.
4. Geelen IGP, Thielen N, Janssen JJWM, Hoogendoorn M, Roosma TJA, Willemsen SP, et al. Treatment outcome in a population-based, 'real-world' cohort of patients with chronic myeloid leukemia. Haematologica. 2017;102(11):1842–9.
5. Stukan I, Gryzik M, Hoser G, Want A, Grabowska-Pyrzewicz W, Zdioruk M, et al. Novel Dicarboximide BK124.1 Breaks Multidrug Resistance and Shows Anticancer Efficacy in Chronic Myeloid Leukemia Preclinical Models and Patients' $CD34^{+}/CD38^{-}$ Leukemia Stem Cells. Cancers (Basel). 2022;14(15):3641.
6. Patnaik MM, Tefferi A. Chronic myelomonocytic leukemia: 2024 update on diagnosis, risk stratification and management. Am J Hematol. 2024;99(6):1142–65.
7. Chan O, Renneville A, Padron E. Chronic myelomonocytic leukemia diagnosis and management. Leukemia. 2021;35(6):1552–62.
8. Wang K, Sun Q, Zhong X, Zeng M, Zeng H, Shi X, et al. Structural mechanism for GSDMD targeting by autoprocessed caspases in pyroptosis. Cell. 2020;180(5):941–55.
9. Zhu C, Xu S, Jiang R, Yu Y, Bian J, Zou Z. The gasdermin family: emerging therapeutic targets in diseases. Signal Transduct Target Ther. 2024;9(1):87.
10. Huang H, Weng Y, Tian W, Lin X, Chen J, Luo L. Molecular mechanisms of pyroptosis and its role in anti-tumor immunity. Int J Biol Sci. 2023;19(13):4166–80.
11. Liu Y, Fang Y, Chen X, Wang Z, Liang X, Zhang T, et al. Gasdermin E-mediated target cell pyroptosis by CAR T cells triggers cytokine release syndrome. Sci Immunol. 2020;5(43):eaax7969.
12. Wang Q, Wang Y, Ding J, Wang C, Zhou X, Gao W, et al. A bioorthogonal system reveals antitumour immune function of pyroptosis. Nature. 2020;579(7799):421–6.
13. Wang Y, Gao W, Shi X, Ding J, Liu W, He H, et al. Chemotherapy drugs induce pyroptosis through caspase-3 cleavage of a gasdermin. Nature. 2017;547(7661):99–103.
14. Liu X, Xia S, Zhang Z, Wu H, Lieberman J. Channelling inflammation: gasdermins in physiology and disease. Nat Rev Drug Discov. 2021;20(5):384–405.
15. Fan JX, Deng RH, Wang H, Liu XH, Wang XN, Qin R, et al. Epigenetics-Based tumor cells pyroptosis for enhancing the immunological effect of chemotherapeutic nanocarriers. Nano Lett. 2019;19(11):8049–58.
16. Tsai HC, Li H, Van Neste L, Cai Y, Robert C, Rassool FV, et al. Transient low doses of DNA-demethylating agents exert durable antitumor effects on hematological and epithelial tumor cells. Cancer Cell. 2012;21(3):430–46.
17. Penter L, Liu Y, Wolff JO, Yang L, Taing L, Jhaveri A, et al. Mechanisms of response and resistance to combined decitabine and ipilimumab for advanced myeloid disease. Blood. 2023;141(15):1817–30.
18. Van Laer L, Huizing EH, Verstreken M, van Zuijlen D, Wauters JG, Bossuyt PJ, et al. Nonsyndromic hearing impairment is associated with a mutation in DFNA5. Nat Genet. 1998;20(2):194–7.
19. Hu J, Dong Y, Ding L, Dong Y, Wu Z, Wang W, et al. Local delivery of arsenic trioxide nanoparticles for hepatocellular carcinoma treatment. Signal Transduct Target Ther. 2019;4:28.
20. Lu H, Zhang S, Wu J, Chen M, Cai MC, Fu Y, et al. Molecular targeted therapies elicit concurrent apoptotic and GSDME-Dependent pyroptotic tumor cell death. Clin Cancer Res. 2018;24(23):6066–77.
21. Shen X, Wang H, Weng C, Jiang H, Chen J. Caspase 3/GSDME-dependent pyroptosis contributes to chemotherapy drug-induced nephrotoxicity. Cell Death Dis. 2021;12(2):186.
22. Matsusaka S, Lenz HJ. Pharmacogenomics of fluorouracil-based chemotherapy toxicity. Expert Opin Drug Metab Toxicol. 2015;11(5):811–21.
23. Zhu L, Ma J, Jia N, Zhao Y, Shen H. Chitosan-coated magnetic nanoparticles as carriers of 5-fluorouracil: preparation, characterization and cytotoxicity studies. Colloids Surf B Biointerfaces. 2009;68(1):1–6.
24. Wang T, Hou J, Su C, Zhao L, Shi Y. Hyaluronic acid-coated Chitosan nanoparticles induce ROS-mediated tumor cell apoptosis and enhance antitumor efficiency by targeted drug delivery via CD44. J Nanobiotechnol. 2017;15(1):7.
25. Sun Y, Zhao D, Wang G, Jiang Q, Guo M, Kan Q, et al. A novel oral prodrug-targeting transporter MCT 1: 5-fluorouracil-dicarboxylate monoester conjugates. Asian J Pharm Sci. 2019;14(6):631–9.
26. Song N, Zhang J, Zhai J, Hong J, Yuan C, Liang M. Ferritin: A multifunctional nanoplatform for biological detection, imaging diagnosis, and drug delivery. Acc Chem Res. 2021;54(17):3313–25.
27. Pang J, Feng X, Liang Q, Zheng X, Duan Y, Zhang X, et al. Ferritin-Nanocaged ATP traverses the Blood-Testis barrier and enhances sperm motility in an asthenozoospermia model. ACS Nano. 2022;16(3):4175–85.
28. Budiarta M, Roy S, Katenkamp T, Feliu N, Beck T. Overcoming Non-Specific interactions for efficient encapsulation of doxorubicin in ferritin nanocages for targeted drug delivery. Small. 2023;19(21):e2205606.
29. Liang M, Fan K, Zhou M, Duan D, Zheng J, Yang D, et al. H-ferritin-nanocaged doxorubicin nanoparticles specifically target and kill tumors with a single-dose injection. Proc Natl Acad Sci U S A. 2014;111(41):14900–5.
30. Li L, Fang CJ, Ryan JC, Niemi EC, Lebrón JA, Björkman PJ, et al. Binding and uptake of H-ferritin are mediated by human transferrin receptor-1. Proc Natl Acad Sci U S A. 2010;107(8):3505–10.
31. Zhao Y, Liang M, Li X, Fan K, Xiao J, Li Y, et al. Bioengineered Magnetoferritin nanoprobes for Single-Dose Nuclear-Magnetic resonance tumor imaging. ACS Nano. 2016;10(4):4184–91.
32. Jiang B, Chen X, Sun G, Chen X, Yin Y, Jin Y et al. A natural drug entry channel in the ferritin nanocage. Nano Today. 2020, 35100948.
33. Ben-Neriah Y, Daley GQ, Mes-Masson AM, Witte ON, Baltimore D. The chronic myelogenous leukemia-specific P210 protein is the product of the Bcr/abl hybrid gene. Science. 1986;233(4760):212–4.
34. Senapati J, Sasaki K, Issa GC, Lipton JH, Radich JP, Jabbour E, et al. Management of chronic myeloid leukemia in 2023-common ground and common sense. Blood Cancer J. 2023;13(1):58.
35. Vener C, Banzi R, Ambrogi F, Ferrero A, Saglio G, Pravettoni G, et al. First-line Imatinib vs second- and third-generation TKIs for chronic-phase CML: a systematic review and meta-analysis. Blood Adv. 2020;4(12):2723–35.
36. Fan D, Cao Y, Cao M, Wang Y, Cao Y, Gong T. Nanomedicine in cancer therapy. Signal Transduct Target Ther. 2023;8(1):293.
37. Zhang J, Cheng D, He J, Hong J, Yuan C, Liang M. Cargo loading within ferritin nanocages in Preparation for tumor-targeted delivery. Nat Protoc. 2021;16(10):4878–96.
38. Huang Q, Li F, Liu X, Li W, Shi W, Liu FF, et al. Caspase 3-mediated stimulation of tumor cell repopulation during cancer radiotherapy. Nat Med. 2011;17(7):860–6.
39. Bhat AA, Thapa R, Afzal O, Agrawal N, Almalki WH, Kazmi I, et al. The pyroptotic role of Caspase-3/GSDME signalling pathway among various cancer: A review. Int J Biol Macromol. 2023;242(Pt 2):124832.
40. Cao W, Chen G, Wu L, Yu KN, Sun M, Yang M, et al. Ionizing radiation triggers the antitumor immunity by inducing gasdermin E-Mediated pyroptosis in tumor cells. Int J Radiat Oncol Biol Phys. 2023;115(2):440–52.
41. Ye F, Zhang W, Fan C, Dong J, Peng M, Deng W, et al. Antileukemic effect of venetoclax and hypomethylating agents via caspase-3/GSDME-mediated pyroptosis. J Transl Med. 2023;21(1):606.

42. Banegas MP, Rivera DR, O'Keeffe-Rosetti MC, Carroll NM, Pawloski PA, Tabano DC, et al. Long-Term patterns of oral anticancer agent adoption, duration, and switching in patients with CML. J Natl Compr Canc Netw. 2019;17(10):1166–72.
43. Senapati J, Jabbour E, Kantarjian H, Short NJ. Pathogenesis and management of accelerated and blast phases of chronic myeloid leukemia. Leukemia. 2023;37(1):5–17.
44. Laskowski TJ, Biederstädt A, Rezvani K. Natural killer cells in antitumour adoptive cell immunotherapy. Nat Rev Cancer. 2022;22(10):557–75.
45. Melenhorst JJ, Chen GM, Wang M, Porter DL, Chen C, Collins MA, et al. Decade-long leukaemia remissions with persistence of $CD4^+$ CAR T cells. Nature. 2022;602(7897):503–9.

Publisher's note